Band Structure Engineering of Carbon Nitride Hybrid Photocatalysts for CO_2 Reduction in Aqueous Solutions

Verity L. Piercy[a][b], Gaia Neri[a], Troy D. Manning[b], Andrea Pugliese[b], Frédéric Blanc[a][b], Robert G. Palgrave,[c] Alexander J. Cowan[a], Matthew J. Rosseinsky[b]

[a] Stephenson Institute for Renewable Energy, University of Liverpool, Liverpool, L69 7ZF, UK

[b] Department of Chemistry, University of Liverpool, Liverpool, L69 7ZD, UK

[c] Department of Chemistry, University College London, London, WC1H 0AJ, UK

FeTCPP modified carbon nitrides were prepared by mechanical mixing. After stirring the suspension was then centrifuged, using a Heraeus Megafuge 16R, to remove the FeTCPP solution and then washed twice with 50 mL ethanol. Powders were then dried overnight at 60 °C.

For ICP-OES measurements, samples were prepared by placing 5 mg of the material in 1 mL ~17 M H_2SO_4 and heating at ~100 °C for 1 hour or until particulates had completely dissolved.

For DRIFTS measurements discs were prepared by dilution in KBr, specifically, 2 mg of sample in 100 mg KBr, mixed by grinding with a pestle and mortar till reaching homogeneity and then loaded into sample well. Spectra were collected at a resolution of 2 cm^{-1} over 64 accumulations and were baselined with a KBr powder in air.

All NMR spectra were recorded on a Bruker DSX 400 MHz NMR spectrometer equipped with a 4 mm HXY probe tuned to X = ^{13}C at 101 MHz and Y = ^{15}N at 40 MHz. Spectra were obtained under Cross Polarisation (CP) Magic Angle Spinning (MAS) conditions. ^{1}H pulses and SPINAL 64 decoupling[1] were performed at a radio frequency (rf) field amplitude of 83 kHz. For the ^{13}C CP step, a 70 – 100 % ramped rf field of 1 ms centred at 35 kHz was applied on ^{13}C, while the ^{1}H rf field was matched to obtain optimum signal at around 66 kHz. For the ^{15}N CP step, a 70 – 100 % ramped rf field of 6 ms centred at 40 kHz was applied on ^{15}N, while the ^{1}H rf field was matched to obtain optimum signal at around 60 kHz. The MAS rates were 10 and 5 kHz for ^{13}C and ^{15}N, respectively. ^{13}C and ^{15}N chemical shift were referenced to CH signal of adamantane at 29.45 ppm[2] and the NH_3^+ signal of glycine at 33.40 ppm[3].

UV-Vis-NIR diffuse reflectance spectroscopy (DRS) data was obtained with a Shimadzu UV-2550 UV/Vis spectrometer, equipped with an integrating sphere, over the spectral range of 200-1400 nm and $BaSO_4$ was used as a reflectance standard.[4] The diffuse reflectance spectra were then converted from reflectance to absorption according to the Kubelka-Munk function:

$$F(R) = \frac{k}{s} = \frac{(1 - R_\infty)^2}{(2R_\infty)}$$

where k and s are absorption and scattering coefficients, respectively and R is the diffuse reflectance based on the Kubelka–Munk theory of diffuse reflectance. The data can then be plotted using the equation:

$$(\alpha h v)^{\frac{1}{n}} = A(h v - E_{BG})$$

where α is the absorption coefficient, h is Planck's constant, v is the frequency of light, A is the proportionality constant and E_{BG} is the band gap. The value of n denotes the nature of the transition, n = ½ for direct transitions or n = 2 for indirect transitions. A Tauc plot of $(\alpha h v)^{\frac{1}{n}}$ versus $h v$ can be used to estimate the band gap of the material by linear extrapolation to find the x-intercept.[4]

UV-Vis spectra of solutions were collected on the same piece of equipment with a standard sample compartment, using a 4 mL (path length, 10 mm) or 0.4 mL (path length, 1 mm) quartz cuvette. Determination of concentrations of soaking samples were determined using the Beer-Lambert equation:

$$A = \varepsilon\, l\, c = log_{10} \frac{I_0}{I}$$

where, A is the absorbance, ε is molar absorptivity, I is the path length, c is the concentration, I_0 is the incident light intensity, and I is the transmitted light intensity.

XPS valance band spectra were measured using a Mg Kα (1253.6 eV) X-ray source operating at 144 W and a hemispherical PSP Vacuum Technology electron energy analyser, operating with a typical constant pass energy of 20 eV. A sputtered polycrystalline Ag sample was used for calibration, to determine the precision of the analyser. The secondary electron cut-off (SEC) at low kinetic energies was measured with the X-ray source operating at 9 W with an applied bias of 10 V between the sample and analyser, to separate the spectrometer response. XPS core level spectra were obtained with a two chamber Thermo Theta Probe spectrometer using a monochromated Al Kalpha X-ray source (1486.6 eV) in constant analyser energy mode. X-rays were focused to a 400 micron spot at the sample surface, which defined the analysis area. Sample charging was prevented by use of a dual beam flood gun. High resolution core line spectra, were recorded at 50 eV pass energy, and survey spectra were recorded at 150 eV pass energy. All XPS spectra were fitted using CasaXPS software which fits spectra using a Gaussian/Lorentzian product function to approximate a Voigt function after Shirley background removal with a binding energy determination precision of $\pm$ 0.1 eV and all spectra were calibrated to an adventitious carbon peak of 284.6 eV.

Steady-State Photoluminescence (PL) and Time-Resolved Emission Lifetime Spectroscopy measurements were recorded on an Edinburgh Instruments FLS980-D2S2-STM spectrophotometer, equipped with a 450 W Ozone free Xe arc lamp, excitation and emission monochromators and a photomultiplier tube detector. Samples were prepared by sandwiching powders in a demountable quartz cuvette (130 µL). Steady-state photoluminescence spectra were collected in air by a single measurement with an excitation wavelength of 390 nm, monitoring between 410 and 700 nm (2 nm step and 0.1 s dwell time).

Time-resolved emission lifetime spectra were obtained from time-correlated single photon counting measurements, in which a single wavelength is monitored over a certain time period. Spectra were acquired with a 371 nm pulsed laser diode (pulse period of 2 µs in air) between 0 and 2000 ns and a stop condition of 10,000 counts. The monitored emission wavelength is specified for each sample in the figure heading. As the instrument has a certain electronic response time, the instrument response function (IRF) of the equipment must be determined by measuring the response of the instrument to a purely scattering solution. The IRF of the instrument was determined using a Ludox sample (aqueous dispersion of silica particles) under the same conditions as those used for the actual samples.

The emission lifetime data was analysed using DecayFit software[5] as this can be used to fit the emission decay to a number of exponential functions, taking the IRF into consideration. The lifetimes were determined by fitting the exponential decay to a multi-component exponential function.

Loading of Pt co-catalyst (1 wt%) onto the surface of materials was performed via photodeposition of H_2PtCl_6 *in-situ*. For *in-situ* experiments, the equivalent amount of H_2PtCl_6 (8 wt% solution) which would provide a maximum of 1 wt% loading (1 mL:0.5 µL, water:H_2PtCl_6 8 wt% solution), v:v) was added to the photocatalyst suspension, purged with N_2 for 30 minutes and placed under illumination, with gas evolution monitored by gas chromatography (GC).

Isotopic labelling experiments were performed using a similar procedure to the typical photocatalytic experiments in which the photocatalyst was placed in a hole scavenger containing solution in a

concentration of 1 mg/mL and then illuminated with visible light for 4-24 hours. The only variation from the typical photocatalysis procedure was the way in which the suspensions were purged; samples were first purged with N_2 for 30 minutes and then purged with $^{13}CO_2$ for several minutes before being placed under illumination. The headspace of the experiment was sampled using a gas syringe, the sample was then injected into a special made pre-purged cell and the FTIR spectra was measured at a resolution of 0.5 cm^{-1} and averaged over 200 accumulations. The cell used for FTIR measurements consisted of a tube with CaF_2 windows attached to either end and a septa port for purging and sample injection.

Table S 1 - Elemental compositions, calculated C:N molar ratios and normalised composition of each carbon nitride.

Material	Measured Mass (%)			C:N (molar ratio)	Composition (Normalised)
	C	H	N		
CN-DCDA	34.84	1.83	61.30	0.663	$C_{0.31}H_{0.20}N_{0.47}O_{0.01}$
CN-BA (5)	35.53	1.74	61.52	0.674	$C_{0.32}H_{0.19}N_{0.48}O_{0.01}$
CN-BA(10)	36.12	1.75	60.55	0.696	$C_{0.33}H_{0.19}N_{0.47}O_{0.01}$
CN-BA(20)	37.28	1.79	59.05	0.736	$C_{0.34}H_{0.19}N_{0.46}O_{0.01}$

*Oxygen content was estimated from balance.

Elemental analysis (CHN) results are summarised in Table S 1. Elemental analysis is used to quantify C, N content as alternative surface sensitive techniques such as XPS are complicated by the presence of additional adventitious carbon. The CHN results reveal that each of the materials have C:N ratios much lower than theoretical g-C_3N_4 (0.75) and are closer to that of the polymer melon (0.68), inferring that the materials are not fully polymerised and are likely rich in defects.[6–15] Furthermore, each of the carbon nitrides contains a small amount of hydrogen, between 1.64-1.92 %. The presence of hydrogen indicates potential moisture in the samples but also incomplete polymerisation of the carbon nitrides, likely due to the existence of amine groups, which can terminate the carbon nitride sheets or exist as defects within the structure.[6,10,14–19] It can be seen that by increasing the barbituric acid content from CN-DCDA to CN-BA(20) that the C:N ratio decreases showing that the copolymerization creates more nitrogen deficient species with increased carbon content. This is due to the ring within barbituric acid containing a carbon in the usual position of a nitrogen in a typical carbon nitride melem repeating unit. This was expected as this has previously been reported.[16,20–26]
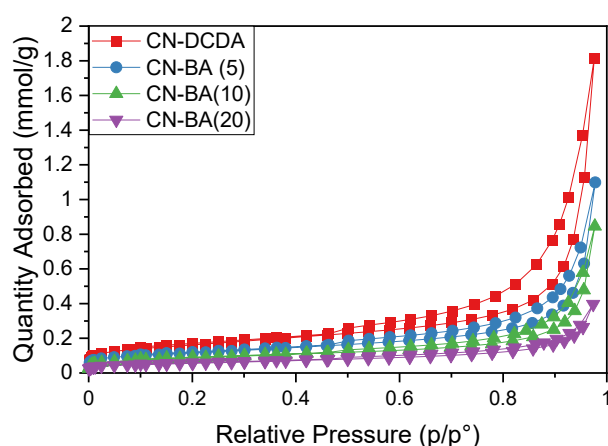

Figure S 1 – N$_2$ Adsorption/desorption isotherms of CN-DCDA, CN-BA(5), CN-BA(10), CN-BA(20).

Table S 2 – Measured BET Surface Area.

Material	Surface Area (m^{2}g^{-1}) [a]
CN-DCDA	12.81
CN-BA (5)	9.04
CN-BA(10)	6.79
CN-BA(20)	4.41

[a] BET surface area calculated over the pressure range (P/P$_0$) 0.05-0.3.

According to the International Union of Pure and Applied Chemistry (IUPAC) surface area and pore size classification, the carbon nitrides all show type IV isotherms with type H3 hysteresis loops, which are characteristic of mesoporous materials consisting of platelet-like particle aggregates, forming slit shaped pores (Figure S 1).[27,28] Across the CN-BA series, there is a decrease in surface area with increasing barbituric acid content (CN-DCDA > CN-BA(5) > CN-BA(10) > CN-BA(20)).
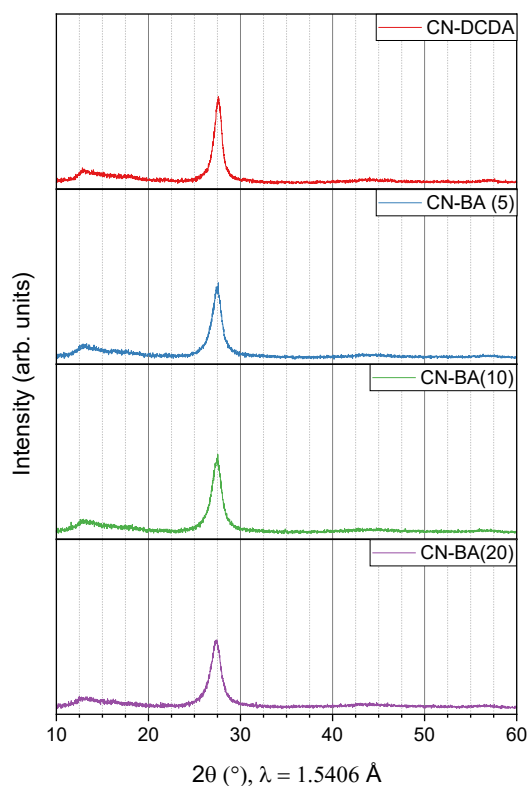

Figure S 2 – PXRD Patterns for CN-DCDA, CN-BA(5), CN-BA(10) and CN-BA(20).

Table S 3 – PXRD Peak position and d-spacing values.

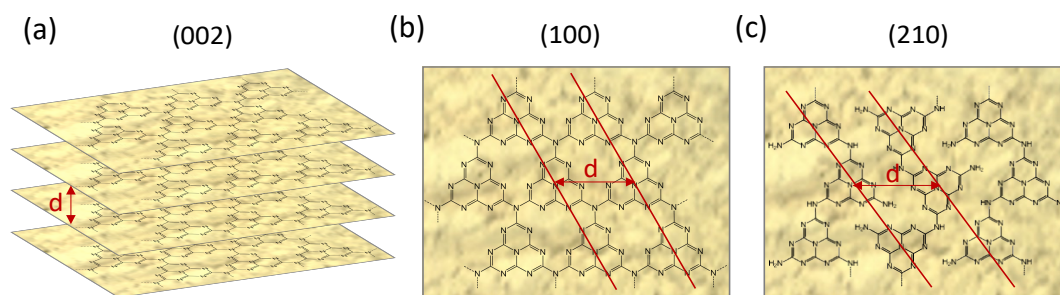| Material	(100) / (210)		(002)		
	2Θ (°)	d-spacing (nm)[a]	2Θ (°)	d-spacing (nm)[a]	FWHM[b]
CN-DCDA	12.9	0.688	27.6	0.323	0.969
CN-BA (5)	12.8	0.691	27.5	0.324	1.090
CN-BA(10)	12.9	0.688	27.5	0.325	1.215
CN-BA(20)	12.7	0.699	27.4	0.326	1.302

Figure S 3 - Depiction of indexed planes in (a) and (b) fully polymerised carbon nitride and melon (c).

The PXRD patterns of all the carbon nitrides can be found in Figure S 2. All materials exhibit two broad features at 2Θ = ~13° and ~27°, these are characteristic peaks of carbon nitride and are consistent with their semi-amorphous nature. The patterns show that there is some long-range ordering due to the presence of the sharper peak at 2Θ = ~27° in most samples. The peak at 2Θ = ~27° is reported as the (002) plane and is assigned as the interplanar distance of the stacked aromatic systems.[7,9,29–40] The stacking distance of the carbon nitride sheets can be estimated using the Bragg equation ($n\lambda = 2d \sin \theta$) and ranges from 0.323 – 0.326 nm for the carbon nitrides. Generally, the peak at 2Θ = ~13° is assigned to the in-plane structural packing motif of the carbon nitride heterocycles and in this work is determined to have a distance between 0.661 nm and 0.699 nm. These values are only slightly below that of the size of a single heptazine unit (0.713 nm), which has previously been attributed to a small tilt or buckling of the units to minimise repulsion between nitrogen lone pairs.[6,16,32,41–45] A number of groups have attempted to assign a single structure to the carbon nitride, however, due to the broadness of the peak it is unlikely that a single structure can be allocated, and these materials cannot be considered as an overall homogeneous phase, instead it is likely that numerous structures exist within the materials varying from melon type structures to more fully polymerised motifs.[34933]It can be seen that the d-spacing values for the peak at 2Θ = ~13° decrease with increasing amounts of barbituric acid used in the synthesis of the carbon nitrides. This is generally considered to be due to the incorporation of the barbituric acid motif introducing C into the heptazine structure creating disturbance in the carbon nitride network and weakening the H-bonding network, disrupting long range ordering.[16,21] Also for this series of materials, there appears to be a general shift in the 2Θ = ~27° peak to lower values, a

decrease in intensity and increase in peak broadening (FWHM) indicating further disturbance in the graphitic structure.[16,21]

All carbon nitrides within this work showed the usual reported characteristic FTIR stretches at ~3500-2800 cm^{-1}, ~1200-1700 cm^{-1} and ~810 cm^{-1}, usually assigned to amine groups, CN heterocycles and CN ring breathing modes, respectively, a full list of approximate peak positions and assignments for Figure S 4, can be found in Table S 4. The broad peaks ~2900-3500 cm^{-1} are assigned to the overlap of stretching vibrations of -OH groups and –NH/-NH$_2$ vibrations implying the presence of surface amino groups. The presence of these amino groups further indicates incomplete polymerisation. The broadness of the bands is attributed to adsorbed water.[19,46–51] As this broad region extends to much lower wavenumbers than usual, this could indicate the presence of C-H stretches, which is a further indication of incomplete polymerisation, however this is difficult to definitively assign. The broad band has also previously been attributed to H-bonding or other interaction effects, but could be due to amine groups situated in different environments which may include triazine or heptazine rings but also incomplete ring structures.[38] Within the ~1200-1700 cm^{-1} there are a number of relatively sharp peaks, generally these are assigned as C-N heterocycles but some reports assign peaks to not only stretching vibrations of the C=N and C-N in the aromatic heptazine heterocycles[52,55,62,65,66,74,75], but also stretching vibrations of C-NH-C and N(C)$_3$ bridging units.[37,51,58,63,76,77] This further indicates a lower degree of polymerisation closer to that of melon than fully condensed graphitic carbon nitride due to defective condensation of the CN framework. The peak at ~810 cm^{-1} is assigned to the breathing mode of the triazine units and/or/within the tri-s-triazine repeating units in the carbon nitride materials.[37,42–44,46–49,52–54,57] A weak peak at ~890 cm^{-1} can be assigned to the deformation mode of N-H.[30,46,50,61] Another weak peak at ~2100-2200 cm^{-1} is assigned to -C≡N groups and is likely caused by incomplete polymerisation of DCDA in each sample. The only shift that can be observed is a slight shift in position for the peak at ~810 cm^{-1}, from 809 cm^{-1} to 813 cm^{-1}, which may be indicative of carbon being introduced into the rings and causing some distortion in the heterocycle. Also, within this series, with increasing amounts of barbituric acid used, peaks become broader and less defined, and the peaks centred at ~810 cm^{-1} and ~890 cm^{-1} decrease in intensity, which may also indicate increased disorder, due to incorporation of carbon into the structure.
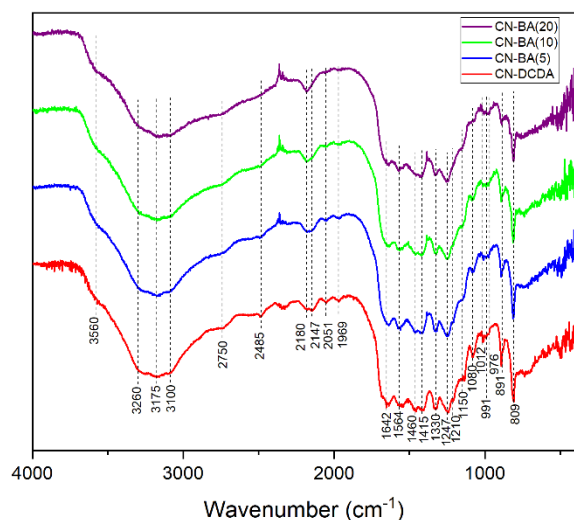

Figure S 4 - DRIFTS for CN-DCDA, CN-BA(5), CN-BA(10) and CN-BA(20). Dotted lines are included as a guide to the eye

Table S 4 – DRIFTS assignments
[a] peak descriptions: s = strong, ms = medium strong, w = weak, b = broad, sh = shoulder, *Potential assignments are italicised.*

| Wavenumber Region (cm^{-1})	Approximate Wavenumber (cm^{-1}) [a]	Assignment	References
~2400-3600	3560 (*sh*) 3260 (*ms, b*) 3175 (*ms, b*) 3100 (*ms, b*) 2750 (sh) 2509 (sh) 2485 (w)	-OH stretches –NH/-NH$_2$ stretches *-CH stretches*	19,46–51
~2400-2200	-	Atmospheric CO_2	30,42,46,50,52
~2100-2200	2180 (*w*) 2147 (*w*)	-C≡N stretches *-N=C=N- stretches*	46,52–59
~1900-2100	2051 (*w*) 1969 (*w*)	*C=C=C, C=N=C, C=C=N*	46,60
~1200-1700	1642 (*s*) 1564 (*s*) 1460 (*s*) 1415 (*s*) 1330 (*s*) 1247 (*s*) 1210 (*sh*)	C-N heterocycle stretches including: C=N and C-N stretches C-NH-C and N(C)$_3$ bridging units *-C(=O)-N-, C=C, C-OH,* *-C=C=N-,* *-C=N=N-, -C-O-C-*	7,9,11,16,19,30,37,40,42–44,46–59,61–77
~900-1200	1150 (*sh*) 1080 (*ms*) 1012 (*w*) 991 (*w*) 976 (*w*)	*C=C, C-H*	46,60
~890	891 (*ms*)	N-H deformation mode	30,46,50,61
~810	809 (*s*)	Out-of-plane bending mode of triazine/heptazine rings	7,9,11,16,19,30,37,40,42–44,46–59,61–73
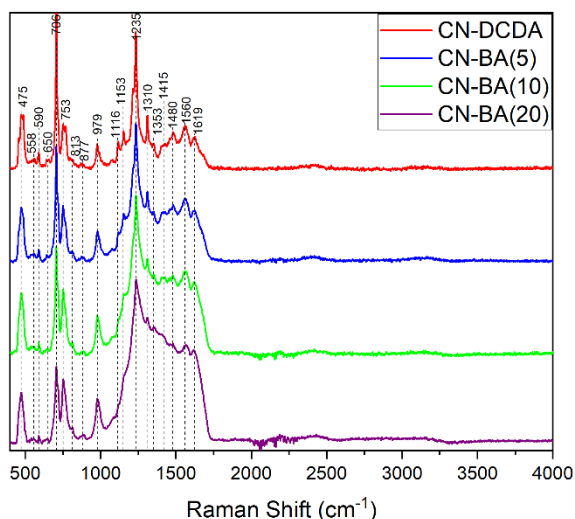
Figure S 5 - FT Raman spectra of CN-DCDA, CN-BA(5), CN-BA(10) and CN-BA(20). Dotted lines are included as a guide to the eye

Table S 5 - Raman assignments for CN-DCDA, CN-BA(5), CN-BA(10) and CN-BA(20).

Raman Shift Region (cm⁻¹)	Approximate Raman Shift (cm⁻¹) [a]	Reported Characteristic Shifts (cm⁻¹)	Assignment
~400-700	475 (s) 558 (w) 590(s)	470 [42,78–83] 550 [78,79] 590 [78,80–83]	Unassigned
~600-900	650 (w) 706 (s) 753 (s)	705 [42,78–83] 750 [42,78–83]	In-plane bending of triazine/heptazine rings [60,78,83–88]
~900-1300	813 (w) 877 (w) 979(s) 1116 (s) 1153 (s) 1235 (s)	980 [78,80–83] 1150 [78,80,83] 1250 [42,78–83]	Symmetric N-breathing mode [60,83–85,87–89] sp² C/ C-N / C=N / N-C=N [46,60,79,82,90]
~1300-1700	1310 (s) 1353 (s) 1415 (w) 1480 (s) 1560 (s) 1619 (s)	1480 [78–83] 1570 [78,79,81] 1620 [42,78–83]	D and G Bands [45,83,84,86,87,89,91–94] sp² C / C-N / C=N / N-C=N [46,56,60,82,95,96]
~2300	-	-	-C≡N / -N=C=N- [46,53,60,87,88,93,96–98]
~3200	-	-	NHₓ / water [46,60]

Peak positions and assignments for Figure S 5 can be found in Table S 5. The vibrational modes at approximately 705 cm⁻¹ and 750 cm⁻¹ are typically assigned to the in-plane bending of C-N-C linkages

within triazine or heptazine rings[60,78,83–88] and the mode at 980 cm^{-1} is attributed to the symmetric N-breathing mode within triazine or heptazine rings.[60,83–85,87–89] Peaks within the 1300-1700 cm^{-1} region are often said to resemble the D and G bands within graphitic materials.[45,83,84,86,87,89,91–94] But it is likely that the modes which lie between 1100-1700 cm^{-1} could be assigned to a range of things including; sp^2 C, C-N, C=N and N-C=N stretches.[46,56,60,79,82,90,95,96]. Sometimes very broad and very weak peaks at higher wavenumber are observed within the Raman spectra, around 2300 cm^{-1}, peaks are assigned to -C≡N or -N=C=N-[46,53,60,87,88,93,96–98] and around 3400 cm^{-1} can be attributed to N-Hx groups or adsorbed water.[46,60] The CN-BA series all show the same vibrational modes, without any significant shift in position across the series. However, we do see clear differences between samples with a variation in intensity and width of peaks. As more barbituric acid is added, the peaks between 1100 and 1700 cm^{-1} become broader, decreasing the resolution of close lying vibrational modes and the intensity of the Raman scattering of these modes also increases from CN-DCDA down to CN-BA(20). These modes are typically assigned to the ring (sp^2) modes and the increased scattering correlates with an expected increase in disorder of the carbon nitride structure due to the increased amount of barbituric acid being incorporated into the structure. Increased Raman scattering is sometimes used as an indicator of increased delocalisation of electrons within organic polymers, however further studies would be required to confirm this hypothesis.[99,100] Interestingly the vibrational mode centred at 705 cm^{-1}, decreases in intensity with increasing BA content. A similar mode was also observed in the DRIFTS data (Figure S 4 and Table S 4) and was assigned to the disruption of the breathing modes of the triazine/ heptazine rings.

The ^{13}C CP MAS NMR of both CN-DCDA and CN-BA(20) samples are similar to previous reports on DCDA and BA copolymerised samples (Figure 2 main text, Table S 6 and S 7).[16,21–23,108] A new peak is observed at 94 ppm for the CN-BA(20) sample, which is not observed in the CN-DCDA material, indicating the existence of a new carbon environment. This can been assigned to protonated carbon confirming the incorporation of carbon into the carbon nitride structure, without disruption to the heptazine based structure.[16,21–23,108] In CN-BA(20), the ^{13}C CP MAS NMR spectrum exhibits broader peaks which are potentially indicative of lower level of crystallinity compared with CN-DCDA.[22] However, the presence of carbonyl groups as indicated by XPS, or C-H as indicated by DRIFTS could not be confirmed, as they lie at a similar shift to the C-N heterocycle peaks and, if present, are likely below the detection limit of ^{13}C NMR or too mobile for CP detection.

Table S 6 - Table of assignments for ^{13}C CP MAS NMR spectra.[9,53,127,128]

Sample	δ (ppm)	Assignment	Width of the half-height (Hz)
CN-DCDA	157	C^e	310 (5)
	163	C^a	190 (20)
	165	C^b and C^c	320 (20)
CN-BA(20)	94	C^d	650 (40)
	157	C^e	540 (25)
	163	C^a	440 (20)
	165	C^b and C^c	340 (10)

Table S 7 - Table of assignments for ^{15}N CP MAS NMR spectra.[9,53,127,129,130]

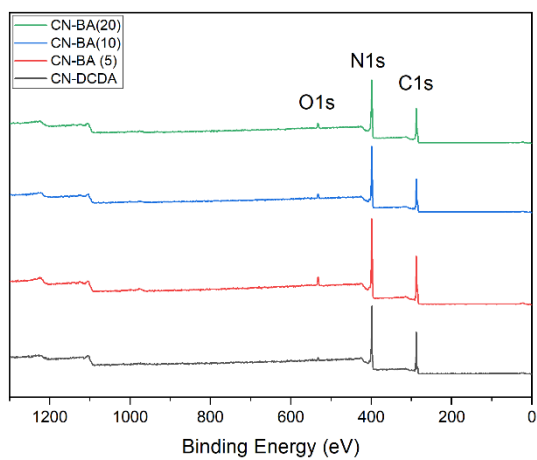| Sample	δ (ppm)	Assignment	Width of the half-height (Hz)
CN-DCDA	108	N^d	550 (40)
	117	N^e	350 (15)
	136	N^c	220 (20)
	155	N^f	220 (30)
	192	N^b	500 (10)
	203	N^a	430 (10)
CN-BA(20)	108	N^d	900 (15)
	117	N^e	770 (50)
	136	N^c	340 (15)
	155	N^f	210 (25)
	192	N^b	690 (40)
	203	N^a	870 (45)

Figure S 6 – XPS survey spectra CN-DCDA, CN-BA(5), CN-BA(10) and CN-BA(20).
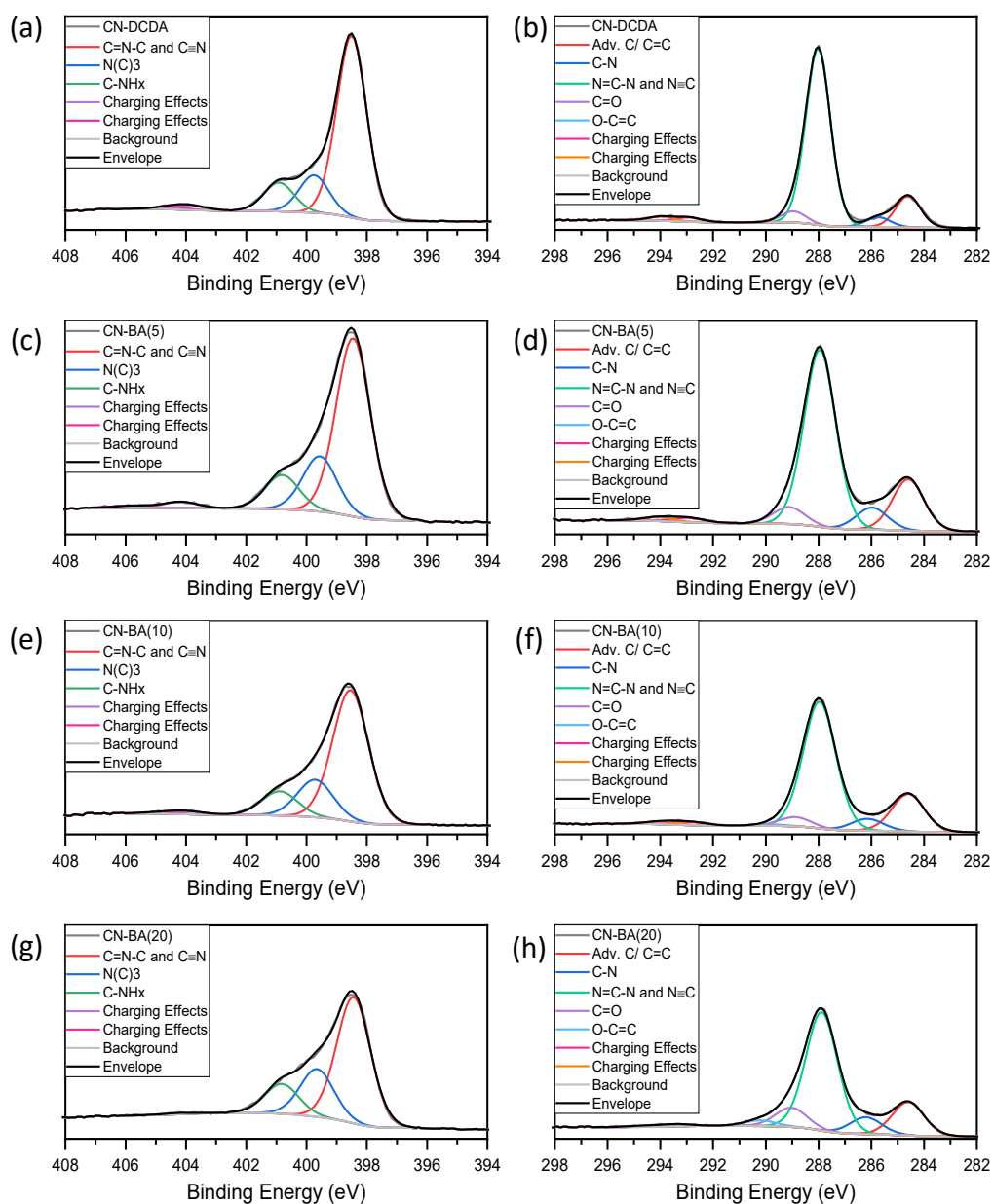
Figure S 7 - High resolution deconvolution of N1s (left) and C1s (right) spectra for (a), (b) CN-DCDA, (c), (d) CN-BA(5), (e), (f) CN-BA(10) and (g), (h) CN-BA(20).

Table S 8 - Deconvolution of N1s peak positions and assignments.

Peak Position (eV)	Assignment		Reference
398	N^a and N^f	(C-N=C)	10,11,21,23,25,30,35,38,43,48–50,56,62,66,89,101–106
399	N^b and N^c	N (N-(C)$_3$)	10,11,21,23,25,30,35,38,43,48–50,56,62,66,89,101–108
401	N^d and N^e	N-Hx	10,11,21,23,25,30,35,38,43,48–50,56,62,63,66,89,101–108
404	π excitations and charging effects		10,21,23,25,30,35,48–50,59,66,89,101,103,104,106,108,109

Table S 9 - Deconvolution of C1s peak positions and assignments.

Peak Position (eV)	Assignment		Reference
284.6	C^d and C^f	adventitious carbon (C-C, C=C, C-H, C=C-H)	40,73,201,202,74,75,95, 115,120,121,168,200
286	C^b and C^c	C-NH_x	25,43,56,103,105,106,110,112–118
288	C^a and C^e	N-C=N, C≡N	40,73,195–202,74,75,95, 115,120,121,168,194
289	C-O, C=O, N-C=O		43,56,85,89,111,116,119
290	O-C=O		113,117
293	π excitations and charging effects		109,110

Deconvolution of the high resolution N1s spectra (Figure S 7) for all materials imply the existence of three N species. The peaks centred at ~398, ~399 and ~401 eV can be assigned to; the sp^2-hybridised N (C-N=C) within the heptazine rings (N^a, Figure 1), tertiary N (N-(C)$_3$) that bridge between and lie at the centre of the heptazine rings (N^b and N^c, Figure 1) and N-Hx in primary and secondary amine groups (N^d and N^e, Figure 1), respectively.[10,11,21,23,25,30,35,38,43,48–50,56,62,66,89,101–106,112–115,117,118]

DRIFTS measurements indicated the presence of C≡N groups (N^f, Figure 1), in XPS these groups are usually found at ~398 eV, which lies at a very close binding energy to sp^2-hybridised N (C-N=C).[117] It is likely that from the N1s spectra we are unable to deconvolute the nitrile peak from the large aromatic N peak. The broad peak found at ~404 eV in the N1s spectra can be attributed to π excitations, charging effects or positive charge localisations in the heterocycles.[10,21,23,25,30,35,48–50,59,66,89,101,103,104,106,108,109,112] A similar peak at ~ 293 eV in the C1s spectra is also assigned to these charge effects.

Reports of the C1s spectra in the literature are much less consistent in terms of peak positions and assignments. Previous studies have fitted the spectra to only two peaks, referring only to the adventitious carbon and the sp^2-hybridised carbon in the aromatic rings at ~284 eV and 288 eV respectively.[21,47,50,93,98,101,104,108,120–125] However, in this work (Figure S 7), the spectra could be deconvoluted to four peaks centred at 284.6, ~286, ~288 and ~289 eV with the development of a fifth peak at ~290 eV, with increasing amounts of barbituric acid in samples CN-BA(10) and CN-BA(20). The first peak at 284.6 eV is assigned to adventitious carbon adsorbed onto the surface of the material and any sp^3 carbon formed during pyrolysis including C-C, C=C and C-H species.[11,25,30,38,43,56,103–106,110–115,117,118] From this XPS data it is not possible to differentiate between the adventitious and sp^3 carbon, despite DRIFTS indicating the potential presence of sp^3 carbon. The incorporation of C=C-H functionality (C^d, Figure 1) that is added due to the use of barbituric acid within the precursor mixture, likely lies within this peak at 284.6 eV and cannot be deconvoluted. The most intense peak at ~288 eV is assigned to the N-C=N aromatic carbon in the heptazine ring (C^a, Figure 1).[11,25,30,38,43,56,103–106,110–115,117,118] Also, much like the N1s spectra, any C≡N groups lie at a similar binding energy to the N-C=N carbon so cannot be deconvoluted.

The peak centred at ~286 eV has previously been reported as a number of different species including; C-O[42,49,62,107,110,111,126] and N=CH-N[22,102], but in this work is attributed to C-N in the primary and secondary amine groups (C^b and C^c, Figure 1).[25,43,56,103,105,106,110,112–118] The peak at ~289 eV can be attributed to C-O/C=O [117,118], though the DRIFTS data appears to show no C=O stretches in the usual region of ~1700 cm^{-1}, it is more likely that this is due to amide groups and/or bound CO_2, as the carbonyl stretches in these groups are at lower wavenumbers and may be masked by the aromatic C-N stretches in the 1500-1700 cm^{-1} region. The peak at ~290 eV can be assigned to O-C=O[113,117], much like the amide groups, the carboxylate are probably difficult to distinguish from the aromatic C-N

stretches in the DRIFTS. Also DRIFTS measurements look at the bulk material, XPS only looks at the surface, so any oxygen species may be at higher concentrations at the surface than in bulk, so are not strong enough to be observed by other techniques as the bulk swamps the signal. These oxygenated groups may in part be due to adsorbed water/CO_2, calcination in air leading to oxygen containing intermediates or species and the incorporation of barbituric acid moieties containing three carbonyl groups.[11,49,62]
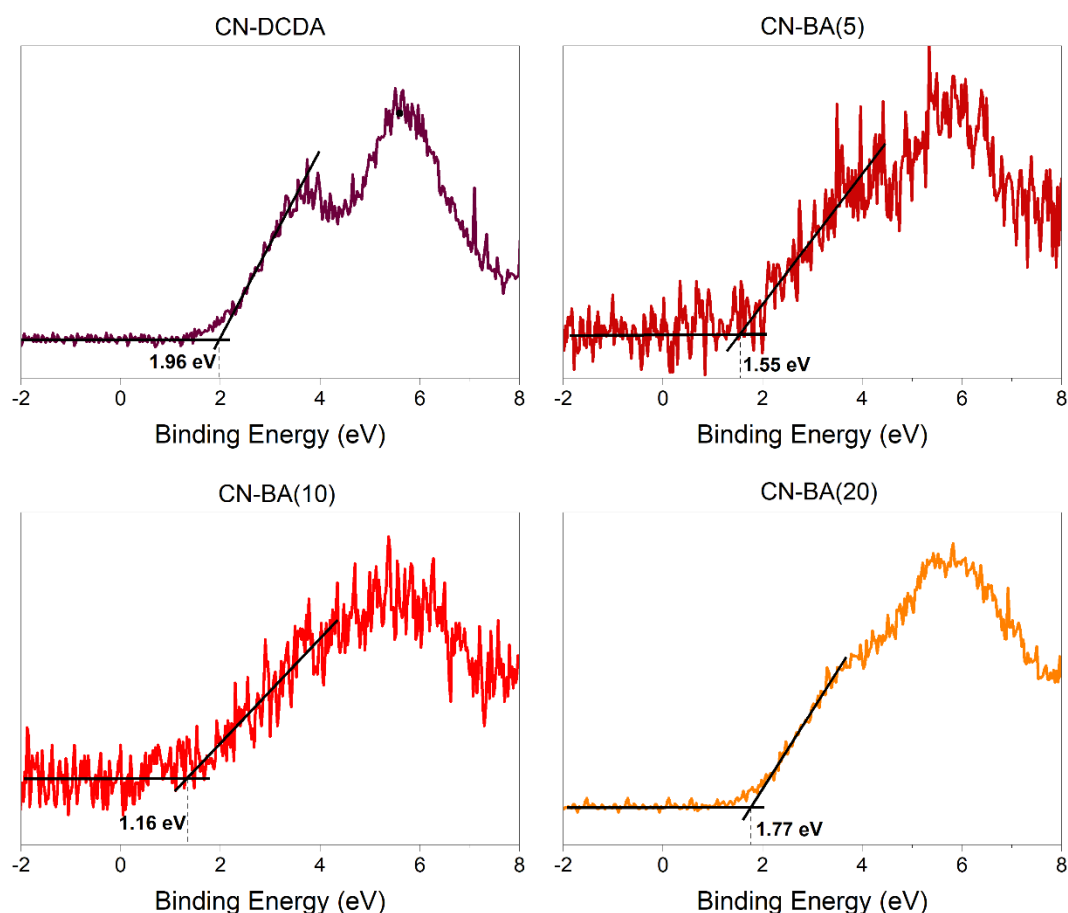
Figure S 8 - XPS Valence band spectra for (a) CN-DCDA, (b) CN-BA(5), (c) CN-BA(10) and (d) CN-BA(20).

Table S 10 Band gap, valence band maximum (VBM) relative to the fermi level, work function (WF) and conduction band (CB) and valence band (VB) position vs vacuum level for CN-DCDA, CN-BA(5), CN-BA(10) and CN-BA(20).

Sample	Band Gap (eV)	XPS VBM (eV)	XPS WF (eV)	VB vs vacuum level (eV)	CB vs vacuum level (eV)
CN-DCDA	2.69	1.96	4.03	5.99	3.31
CN-BA(5)	2.40	1.55	4.03	5.58	3.18
CN-BA(10)	2.21	1.16	4.05	5.21	3.00
CN-BA(20)	1.92	1.77	4.06	5.83	3.91

Figure S 9 - (a) steady state PL emission spectra and (b) time-resolved emission spectra for CN-DCDA, CN-BA(5), CN-BA(10) and CN-BA(20). Excitation at 390 nm for steady-state PL emission. For time-resolved emission, excitation at 371 nm, monitoring emission at, 465, 485, 495 and 495 nm for CN-DCDA, CN-BA(5), CN-BA(10) and CN-BA(20), respectively.
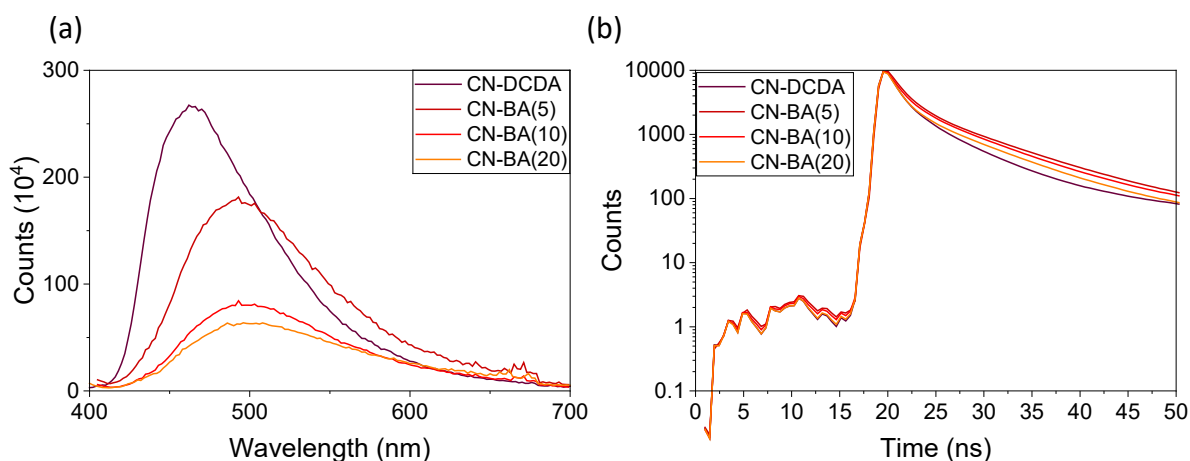
Table S 11 – Radiative lifetimes for HSA carbon nitrides.

Material	τ_1[a] (ns) (A_1 (%))	τ_2 (ns) (A_2 (%))	τ_3 (ns) (A_3 (%))	τ_4 (ns) (A_4 (%))	AWAL[b] (ns)
CN-DCDA	1.58 (0.81)	6.80 (0.18)	46.01 (0.01)	603.33 (0.0002)	2.98
HSA-CN-DCDA	2.40 (0.81)	9.29 (0.18)	61.90 (0.01)	760.50 (0.0003)	4.36
HSA-CN-DCDA/FeTCPP	1.43 (0.77)	5.93 (0.22)	42.63 (0.01)	619.52 (0.0002)	2.81
CN-BA (5)	1.71 (0.74)	8.40 (0.25)	64.48 (0.01)	1373.00 (0.0006)	4.68
HSA-CN-BA(5)	1.72 (0.74)	9.20 (0.26)	66.01 (0.01)	1588.10 (0.0007)	5.15
HSA-CN-BA(5)/FeTCPP	1.20 (0.77)	7.07 (0.22)	46.10 (0.01)	1354.10 (0.0004)	3.34
CN-BA(10)	1.63 (0.75)	8.38 (0.25)	61.42 (0.01)	1437.20 (0.0006)	4.61
HSA-CN-BA(10)	1.44 (0.74)	8.16 (0.25)	51.62 (0.01)	1407.40 (0.0006)	4.45
HSA-CN-BA(10)/FeTCPP	1.04 (0.80)	6.82 (0.20)	49.94 (0.01)	1413.10 (0.0003)	2.86
CN-BA(20)	1.49	8.10	59.05	1424.00	4.48

	(0.74)	*(0.25)*	*(0.01)*	*(0.0006)*	
HSA-CN-BA(20)	1.29	7.23	36.5		2.82
	(0.78)	*(0.21)*	*(0.01)*	[c]	
HSA-CN-BA(20)/FeTCPP	1.55	5.46	33.9		2.89
	(0.74)	*(0.25)*	*(0.01)*		

[a] Emission lifetimes determined by fitting time resolved emission spectra to a 4-component exponential.
[b] Amplitude weighted average lifetimes (AWAL).

[c] These samples were only fitted to 3 time constraints.

The steady-state emission spectra of CN-BA series powders can be seen in Figure S 9(a). CN-DCDA shows a strong broad PL emission around 464 nm, which is typical for most bulk carbon nitrides.[6,30,42,131–133] Upon the addition of barbituric acid this emission maxima then red shifts to 490 nm, which correspond with the decrease in the band gap.[21] Interestingly, as more barbituric acid is incorporated the PL emission shifts but only by a very small amount. It appears that by increasing the amount of barbituric acid in the precursor mixture, that the PL emission is suppressed.[21] This is usually reported to indicate a reduction in charge recombination rates inferring enhanced charge lifetimes, but could also indicate disruption of the conjugated system, which could lead to low charge mobilities and therefore lower recombination rates.[18,21,30,39,62,134] This is likely a result of the increased defect concentration as seen by DRIFTS, Raman and XPS.

Time resolved PL can give information on the lifetimes of free charges that lie near band edges, that recombine to emit light, rather than deep lying states.[135] The radiative lifetimes for each of the materials were determined by fitting the time-resolved fluorescence spectra to a 4-term exponential function corresponding to 4 emissive charge lifetimes. With the addition of barbituric acid in the CN-BA(5) sample. This increase in lifetime can improve the probability that charges will be able to transfer to other species to perform redox reactions before they recombine.[66,72] This enhancement in charge lifetimes could be due to disruption in conjugation due to the incorporation of extra carbon into the CN heterocycles or increased defect concentration, which can lead to lower charge mobility or can act as trap states extending lifetimes. As more BA is incorporated, the produced carbon nitrides have enhanced lifetimes over the CN-DCDA, but the fitted amplitude weighted lifetimes begin to decrease again. A degree of caution is required here as the changes in lifetime between CN-BA(5) and CN-BA(20) are relatively small. But the reduction in the emission intensity as BA levels increase above 5% is clear (Figure S9). As the lifetime of the emission is not changing significantly we conclude that a fraction of the charge recombination must be occurring through less or non-radiative decay from the excited state, which may have been caused by localisation to new states introduced by the BA. [20,56,102,106,136–138]

The PL emission spectra for each of the materials show a large reduction in emission intensity after FeTCPP soaking. The suppression of the emission upon addition of the co-catalyst is indicative of reduced recombination, likely arising from charge transfer from the carbon nitride to the co-catalyst.[36,39,42,43,141,147,148] If we approximate that the photoexcited state has two pathways to decay by (i) emission or (ii) charge transfer to the catalyst, and that both processes can be fitted to a first order (with respect to the CN excited state population, [CN]*) decay then a simple parallel pathway kinetic model can be used where:

$$-\frac{d[CN]^*}{dt} = k_1[CN]^* + k_2[CN]^* = (k_1 + k_2)[CN]^*$$

And it follows that

$$[CN]^*(t) = [CN]^*_0 e^{-k3t} = \underline{[CN]^*_0 e^{-(k_1+k_2)t}}$$

Where k_1 is the rate constant k_1 for decay in the absence of the catalyst approximated to the amplitude weighted lifetime of the PL in the absence of FeTCPP, k_2 is the amplitude weighted lifetime of the PL with the catalyst present and $k_3 = k_1 + k_2$.

The model is for approximation as it has flaws. Namely that (i) it approximates the complex multi-component kinetics of the emissive CN excited state to a single exponential (ii) assumes that electron-transfer is not occurring via an intermediary dark state not observed by PL and (iii) that any change in PL lifetime is due to electron transfer to the FeTCPP and not as a result of any other physical changes brought about as a result of the catalyst absorption process. Nonetheless it is notable that it does lead to an approximately constant rate constant of *ca.* 1.2×10^8 s^{-1} for electron transfer to the FeTCPP in the samples where it is known to be an effective co-catalyst. For the HSA-CN-BA(20) sample the TCPSC lifetime actually increases with the addition of the catalyst, in-line with the photocatalysis results that show minimal CO_2 reduction for this material. The increase in the TCSPC lifetime means it is not possible calculate k_2 and t_2 for this material.

Table S 12 – Time correlated single photon counting (TCSPC) emission amplitude weight average lifetimes (AWAL) for high surface area (HSA) carbon nitrides.

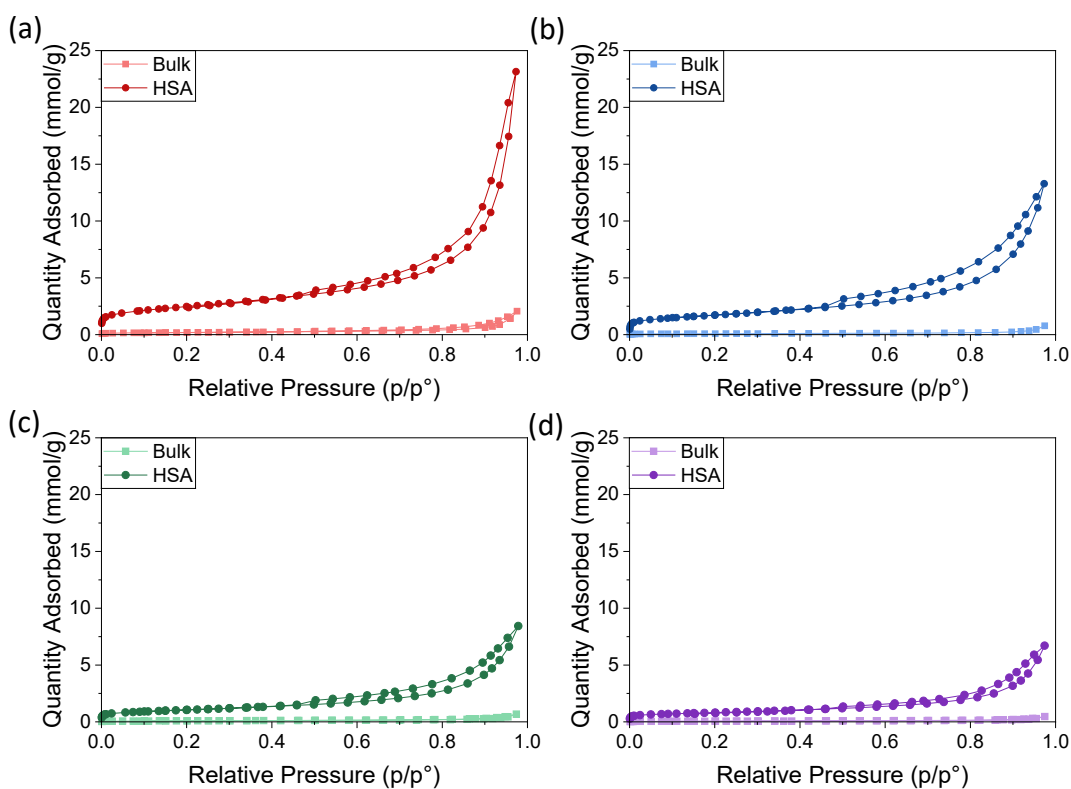| Sample	AWAL (no cat), ns	AWAL (cat), ns	k_1 (10^9 s^{-1})	k_3 (10^9 s^{-1})	k_2 (10^9 s^{-1})	t_2, ns	e-transfer yield
HSA-CN-DCDA	4.36	2.81	0.23	0.36	0.13	7.90	0.36
HSA-CN-BA(5)	5.15	3.34	0.19	0.30	0.11	9.50	0.35
HSA-CN-BA(10)	4.61	2.86	0.22	0.35	0.13	7.53	0.38
HSA-CN-BA(20)	2.38	2.89	0.42	0.35	NA	NA	0.00

Figure S 10 - N₂ adsorption/desorption isotherms of bulk and high surface area (HSA) carbon nitrides. (a) CN-DCDA, (b) CN-BA(5), (c) CN-BA(10) and (d) CN-BA(20)

Due to the need to achieve an appreciable surface loading of co-catalysts for improved photocatalytic activity, an increase in surface area was achieved via thermal exfoliation of the carbon nitride series, characterization of these samples showed little difference when compared with bulk materials (Figure S10-S11 and Table S14-16)

Table S 13 – Measured BET Surface area of the HSA carbon nitrides.

Material	Surface Area (m^2g^{-1})
HSA-CN-DCDA	192.54 (± *26.52*)[b]
HSA-CN-BA(5)	135.45 (± *28.05*)
HSA-CN-BA(10)	82.40 (± *10.66*)
HSA-CN-BA(20)	63.78 (± *1.61*)

[a] BET surface area calculated over the pressure range (P/P₀) 0.05-0.3.
[b] Standard deviation of the BET surface area of the high surface area material repeat synthesis.

Table S 14 – Band gaps of HSA carbon nitrides determined from extrapolation of indirect Tauc plot.

Material	Band Gap (eV)
HSA-CN-DCDA	2.73
HSA-CN-BA(5)	2.21
HSA-CN-BA(10)	2.00
HSA-CN-BA(20)	1.74

Exfoliation of the bulk carbon nitrides to form the high surface area materials leads to enhanced surface area ranging between 13 and 22 times greater. Characterisation of the exfoliated materials via CHN and DRIFTS show very little difference when compared with the bulk material. The UV-vis spectra of the materials show that after exfoliation that the materials band gaps shift slightly but not to any great extent.

Both the bulk and high surface area materials were tested for H_2 evolution in the presence of EDTA hole scavenger and H_2PtCl_6 for in-situ Pt deposition (1 wt% loading). The rates of H_2 evolved after 4 hours of illumination shows that after thermal exfoliation, the materials have greatly enhanced photocatalytic activity, with HSA-CN-BA(5) achieving the highest activity of 234 $\mu mol\ g^{-1}\ h^{-1}$ for H_2 evolution. The high surface area materials have activities 16, 6, 7.5 and 9 times larger than the bulk materials for CN-DCDA, CN-BA(5), CN-BA(10) and CN-BA(20), respectively. Enhancement in photocatalytic activity can be mostly attributed to increase in surface area providing higher amounts of catalytic sites for Pt deposition and H_2 evolution, along with improved charge lifetimes for samples CN-DCDA and CN-BA(5). Furthermore, the trend in activity across the CN-BA series is maintained even after undergoing exfoliation, combined with the small changes in band gap it is likely that the variation in band structure across the series has not been altered much to that of the bulk materials. When normalised to surface area, CN-BA(5), CN-BA(10) and CN-BA(20) show lower rates for the higher surface area materials than the corresponding bulk samples. The enhancement in H_2 evolution rate per surface area for CN-DCDA when exfoliated may arise from the enhancement in charge lifetimes. Whereas the decrease in activity for the samples could be attributed to a number of factors. The barbituric acid materials all see larger differences in composition after exfoliation than the CN-DCDA material, this could indicate the formation of a greater number of defects, which were in too small amounts to be detected via DRIFTS. These defects could act as recombination centres, which provide non-emissive decay pathways for photogenerated charges, hence the PL emission suppression, ultimately resulting in slightly decreased activity. It was noted that during H_2 evolution experiments, EDTA generated significant levels of CO due to its decomposition, therefore all CO_2 reduction experiments used TEOA as hole scavenger.

Table S 15- Estimated theoretical and experimental FeTCPP loadings on high surface area carbon nitrides.

Material	Maximum theoretical loading[a] (µg FeTCPP/ mg CN)	Loading of FeTCPP ICP (µg FeTCPP/ mg CN)	Loading of FeTCPP UV-Vis[b] (µg FeTCPP/ mg CN)	Loading FeTCPP ICP (wt%)
HSA-CN-DCDA	93.8	21	20.9	2.1
HSA-CN-BA(5)	65.7	19	21.4	1.9
HSA-CN-BA(10)	40.1	14	14.6	1.4
HSA-CN-BA(20)	31.1	14	13.4	1.4

[a] Maximum theoretical loading estimated using carbon nitride surface area and the distance between opposite carboxylic acid groups assumed to be the diameter of the FeTCPP molecule.
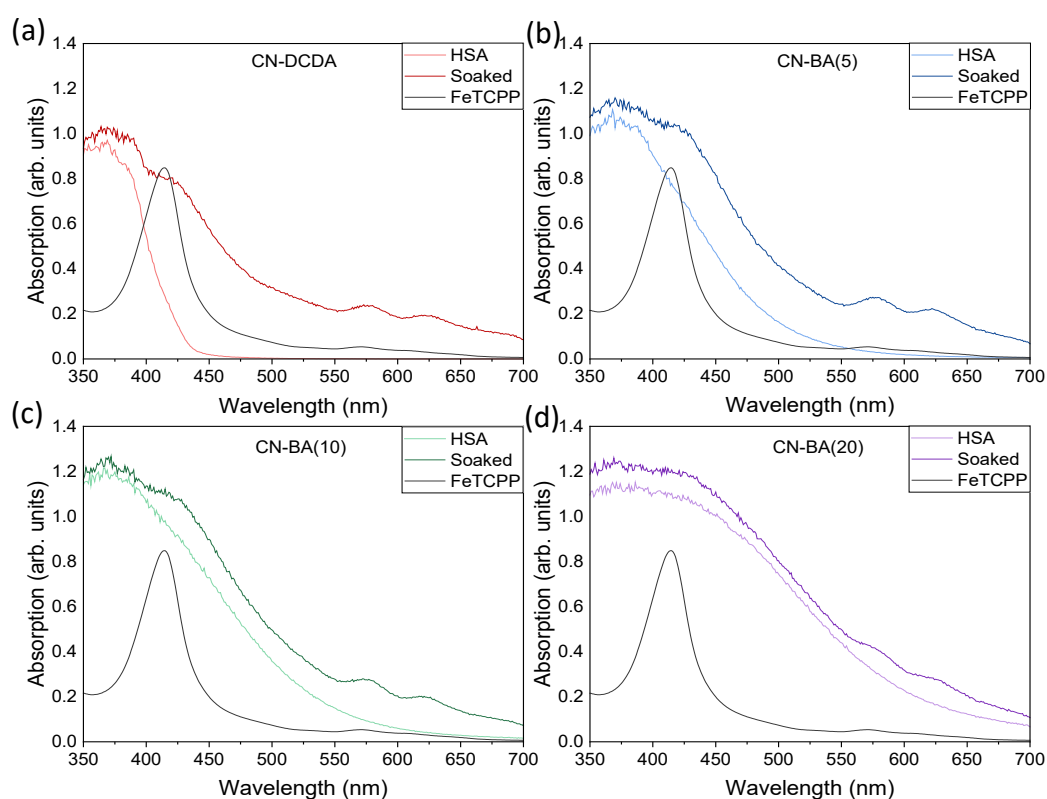[b] Estimated using the Beer-Lambert equation.

Figure S 11 - UV-Vis diffuse reflectance spectra (Kubelka-Munk) of (a) HSA-CN-DCDA, (b) HSA-CN-BA(5), (c) HSA-CN-BA(10) and (d) HSA-CN-BA(20) pre- and post- soaking in FeTCPP solution and UV-Vis spectra of 90 µM FeTCPP ethanolic solution for comparison.

The quantity of the molecular catalyst loaded onto each of the high surface area carbon nitrides was determined by UV-Vis and ICP. UV-Vis spectra of the FeTCPP solutions pre- and post-soaking are shown in Figure S 11 and show characteristic porphyrin bands, with a strong Soret band appearing at 420 nm and weak Q- bands at 532, 572, 618 and 645 nm, attributed to π-π^* transitions.[141–144]
The maximum loading of FeTCPP prior to washing was estimated from the most intense peak at 420 nm using the Beer-Lambert equation (Table S 15). In comparison to the FeTCPP loadings determined by ICP, the values are very close, which indicates that extra washing steps did not lead to desorption

of the catalyst from the carbon nitride surface, at any appreciable level. Despite the large difference in surface area, the materials show similar levels of FeTCPP loading.

The UV-vis spectra the carbon nitrides before and after soaking show extended absorption into the visible range, with clear peaks at 420 nm, 577 nm and 623 nm which can be assigned to the FeTCPP complex. These peaks have been shifted ~ 5 nm from the peaks found for FeTCPP in ethanol, which can be attributed π-π stacking of the FeTCPP on the carbon nitride.[142,143,145,146] Comparison of the DRIFTS spectra before and after soaking do not show the emergence of new peaks that can be assigned to FeTCPP. It appears that the loading of FeTCPP is still too low to be distinguished from the carbon nitride material. Even subtracting the carbon nitride as a baseline does not help to identify new peaks.
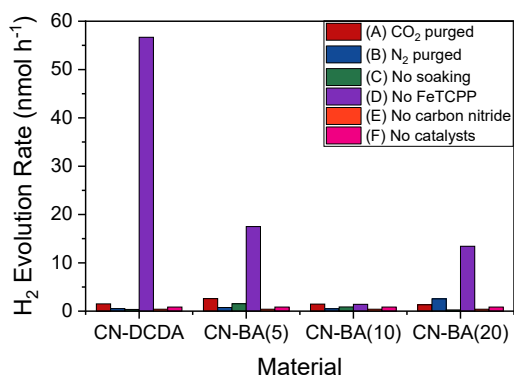

Figure S 12 - H_2 evolution in nmol per hour for 4 mg photocatalyst in 4 ml 10% TEOA (v/v) in water. Samples were purged with N_2 or CO_2 and placed under UV-Vis illumination at ~100 $mWcm^{-2}$ in a quartz-cuvette, for 4 hours on the 300 W Xe lamp set-up. The Xe lamp was equipped with a water filter and a 375 nm long pass filter.

Table S 16 – Conditions for Photocatalytic CO2 reduction

Experiment	Label in Figure S12	CN	FeTCPP	Hole Scavenger	Atmosphere
CN/FeTCPP/10%TEOA/CO2	A	✓	✓	✓	CO_2
CN/FeTCPP/10%TEOA/N2	B	✓	✓	✓	N_2
CN/10%TEOA(25 µM FeTCPP)/CO2	C	✓	✓	✓	CO_2
CN/10%TEOA/CO2	D	✓	✗	✓	CO_2
FeTCPP/10%TEOA/CO2	E	✗	✓	✓	CO_2
10%TEOA/CO2	F	✗	✗	✓	CO_2

Table S 17 - Rates of CO evolution for each of the CN/FeTCPP hybrid materials under different testing conditions.

Experiment	CO Evolution (nmol h^{-1})			
	CN-DCDA	CN-BA(5)	CN-BA(10)	CN-BA(20)
CN/FeTCPP/10%TEOA/CO$_2$	3.156	5.696	2.641	0.350
CN/FeTCPP/10%TEOA/N$_2$	0.061	0.103	0.019	0.139
CN/10%TEOA(25 μM FeTCPP)/CO$_2$	0.096	0.231	0.840	0.063
CN/10%TEOA/CO$_2$	0	0.121	0.163	0
FeTCPP/10%TEOA/CO$_2$	0.085			
10%TEOA/CO$_2$	0			

Table S 18 - Rates of H$_2$ evolution for each of the CN/FeTCPP hybrid materials under different testing conditions.

Experiment	H$_2$ Evolution (nmol h^{-1})			
	CN-DCDA	CN-BA(5)	CN-BA(10)	CN-BA(20)
CN/FeTCPP/10%TEOA/CO$_2$	1.505	2.601	1.458	1.318
CN/FeTCPP/10%TEOA/N$_2$	0.524	0.744	0.498	2.543
CN/10%TEOA(25 μM FeTCPP)/CO$_2$	0.344	1.536	0.875	0.267
CN/10%TEOA/CO$_2$	56.670	17.509	1.404	13.436
FeTCPP/10%TEOA/CO$_2$	0.410			
10%TEOA/CO$_2$	0.851			
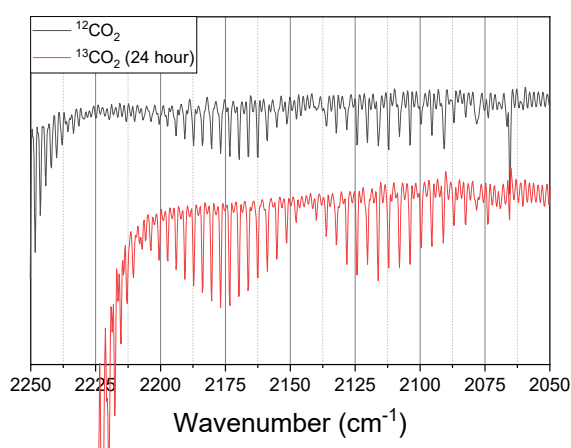
Figure S 13 - FTIR spectra of gas samples taken from photocatalytic experiments purged with $^{12}CO_2$ or $^{13}CO_2$. Conditions of the photocatalytic test; for 10 mg HSA-CN-BA(5)/FeTCPP in 10 ml 10% TEOA (v/v) in water. Samples were purged with N$_2$ for 30 minutes then $^{12}CO_2$ or $^{13}CO_2$ for 2 minutes and placed under UV-Vis illumination at ~200 mWcm^{-2} in a quartz-cuvette, for 24 hours on the 300 W Xe lamp set-up. The Xe lamp was equipped a 375 nm long pass filter

For the isotopic labelling experiment, 10 mg of HSA-CN-BA(5) was placed in 10 mL 10% TEOA in water, first purged with N_2, for removal of O_2, for 30 minutes and then purged with $^{13}CO_2$ for several minutes. The system was then put under illumination (>375 nm and ~200 mWcm^{-2}) for 24 hours before testing the headspace via FTIR. The system was scaled up, with a higher light intensity and longer illuminations times to give the system the best chance to produce as much gas as possible to make it easier to detect via FTIR. For comparison, this experiment was also performed in the presence of $^{12}CO_2$, to confirm the shift in peak positions between ^{12}CO and ^{13}CO.

Figure S 13 shows the results of the FTIR isotopic labelling experiments when purged under $^{12}CO_2$ and $^{13}CO_2$, specifically looking at the CO stretching region. A positive result should show that the CO bands shifted to lower wavenumbers with the Q-branch shifted from ~2150 cm^{-1} under $^{12}CO_2$ to ~2100 cm^{-1} under $^{13}CO_2$. However, the data presented in Figure S 13 shows a small shift of ~4 cm^{-1} to higher wavenumber of the CO stretch.

A similar positive shift in the CO stretch has previously been reported during $^{13}CO_2$ studies by our group.[149] The apparent positive shift in stretching frequency of the Q-branch was found to be due to the presence of both ^{13}CO and ^{12}CO, with the overlapped spectra complicating analysis. By subtracting a scaled ^{12}CO signal away from the ^{13}CO signal, they were able to determine that ~30% of the FTIR signal of the $^{13}CO_2$ experiment was due to ^{12}CO. The source of the ^{12}CO was tentatively attributed to long irradiation times leading to breakdown of the hole scavenger, ascorbate. Shorter periods of illumination saw only minimal amounts of CO evolved in the absence of CO_2 and was found that longer illumination led to a rapid rise in the CO levels. Subtraction of the ^{12}CO from the ^{13}CO was attempted with the data presented here, however no actual ^{13}CO signal could be identified and is likely swamped by the ^{12}CO signal. It is postulated that the source of the ^{12}CO is from TEOA and is thought to be due to degradation of the scavenger forming $^{12}CO_2$ which was preferentially reduced at the catalysts surface over $^{13}CO_2$, which is further away in solution. The small amount of CO produced when experiments were performed under a N_2 atmosphere could be due to TEOA oxidation forming CO_2 as it is consumed for electron donation when performing H_2 evolution. However, TEOA is a widely used scavenger in CO_2 reduction and previous studies have found positive results for isotopically labelled experiments when using TEOA as the hole scavenger. It may take some time to form the $^{12}CO_2$ required for subsequent reduction, which may be swamping the FTIR signal. Shorter illumination times could lead to the formation of ^{13}CO which might be easier to identify via FTIR. To test this, HSA-CN-BA(5) was tested under typical conditions on a scale of 4 mg of photocatalyst to 4 mL 10% TEOA under Xe lamp illuminations with a water filter and 375 nm long pass filter at an intensity of 100 mWcm^{-2} for a much shorter period (4 hours). After 4 hours of illumination, the observed small CO doublet was centred ~2100 cm^{-1} confirming the presence of ^{13}CO. This proves that the CO produced in the first 4 hours of illumination is due to reductions of the purged $^{13}CO_2$ gas. Over longer illumination periods the majority of the CO is formed from the reduction of $^{12}CO_2$ likely produced via the degradation of the TEOA. For evidence of TEOA degradation leading to subsequent CO_2 reduction, this experiment would have to be repeated in the presence of $^{12}CO_2$ and ^{13}C labelled TEOA. Alongside CO and H_2 low levels of CH_4 were also generated after prolonged illumination. CH_4 formation has previously been observed on other Fe porphyrin catalysts, which have been tested for photocatalytic CO_2 reduction in the presence of a photosensitiser and a hole scavenger in acetonitrile.[112,113]

References

1   B. M. Fung, A. K. Khitrin and K. Ermolaev, *J. Magn. Reson.*, 2000, **142**, 97–101.

2   C. R. Morcombe and K. W. Zilm, *J. Magn. Reson.*, 2003, **162**, 479–486.

3   P. Bertani, J. Raya and B. Bechinger, *Solid State Nucl. Magn. Reson.*, 2014, **61**–**62**, 15–18.

4   T. Wada and S. Yamazoe, *Shimadzu Appl. News - Spectrophotometric Anal.*, A428.

5   DecayFit - Fluorescence Decay Analysis Software 1.3, FluorTools, http://www.fluortools.com/software/decayfit.

6   A. Thomas, A. Fischer, F. Goettmann, M. Antonietti, J.-O. Müller, R. Schlögl and J. M. Carlsson, *J. Mater. Chem.*, 2008, **18**, 4893.

7   Y. Zheng, L. Lin, X. Ye, F. Guo and X. Wang, *Angew. Chemie - Int. Ed.*, 2014, **53**, 11926–11930.

8   M. Groenewolt and M. Antonietti, *Adv. Mater.*, 2005, **17**, 1789–1792.

9   B. V. Lotsch, M. Döblinger, J. Sehnert, L. Seyfarth, J. Senker, O. Oeckler and W. Schnick, *Chem. - A Eur. J.*, 2007, **13**, 4969–4980.

10   W. Tu, Y. Xu, J. Wang, B. Zhang, T. Zhou, S. Yin, S. Wu, C. Li, Y. Huang, Y. Zhou, Z. Zou, J. Robertson, M. Kraft and R. Xu, *ACS Sustain. Chem. Eng.*, 2017, **5**, 7260–7268.

11   H. Wang, Z. Sun, Q. Li, Q. Tang and Z. Wu, *J. CO2 Util.*, 2016, **14**, 143–151.

12   E. Wirnhier, M. Döblinger, D. Gunzelmann, J. Senker, B. V Lotsch and W. Schnick, *Chem. - A Eur. J.*, 2011, **17**, 3213–3221.

13   F. Goettmann, A. Fischer, M. Antonietti and A. Thomas, *Angew. Chemie Int. Ed.*, 2006, **45**, 4467–4471.

14   X. Wang, X. Chen, A. Thomas, X. Fu and M. Antonietti, *Adv. Mater.*, 2009, **21**, 1609–1612.

15   Y. Zhang, H. Gong, G. Li, H. Zeng, L. Zhong, K. Liu, H. Cao and H. Yan, *Int. J. Hydrogen Energy*, 2017, **42**, 143–151.

16   J. Zhang, X. Chen, K. Takanabe, K. Maeda, K. Domen, J. D. Epping, X. Fu, M. Antonietti and X. Wang, *Angew. Chemie Int. Ed.*, 2010, **49**, 441–444.

17   Y. Zheng, J. Liu, J. Liang, M. Jaroniec and S. Z. Qiao, *Energy Environ. Sci.*, 2012, **5**, 6717.

18   J. Zhang, M. Zhang, R.-Q. Sun and X. Wang, *Angew. Chemie Int. Ed.*, 2012, **51**, 10145–10149.

19   Y. Wang, J. Hong, W. Zhang and R. Xu, *Catal. Sci. Technol.*, 2013, **3**, 1703.

20   M. Shalom, M. Guttentag, C. Fettkenhauer, S. Inal, D. Neher, A. Llobet and M. Antonietti, *Chem. Mater.*, 2014, **26**, 5812–5818.

21   J. Qin, S. Wang, H. Ren, Y. Hou and X. Wang, *Appl. Catal. B Environ.*, 2015, **179**, 1–8.

22   E. Vorobyeva, Z. Chen, S. Mitchell, R. K. Leary, P. Midgley, J. M. Thomas, R. Hauert, E. Fako, N. López and J. Pérez-Ramírez, *J. Mater. Chem. A*, 2017, **5**, 16393–16403.

23   L. Li, Q. Meng, H. Lv, L. Shui, Y. Zhang, Z. Zhang, Z. Chen, M. Yuan, R. Nötzel, X. Wang, J.-M. Liu and G. Zhou, *Appl. Surf. Sci.*, 2018, **428**, 739–747.

24   M. Ning, Z. Chen, L. Li, Q. Meng, Z. Chen, Y. Zhang, M. Jin, Z. Zhang, M. Yuan, X. Wang and G. Zhou, *Electrochem. Commun.*, 2018, **87**, 13–17.

25 G. Li, Q. Wang, Y. Wu, Y. Li and L. Guo, *Spectrochim. Acta - Part A Mol. Biomol. Spectrosc.*, 2019, **215**, 307–312.

26 C. Zhou, C. Lai, P. Xu, G. Zeng, D. Huang, Z. Li, C. Zhang, M. Cheng, L. Hu, J. Wan, F. Chen, W. Xiong and R. Deng, *ACS Sustain. Chem. Eng.*, 2018, **6**, 6941–6949.

27 M. Thommes, K. Kaneko, A. V. Neimark, J. P. Olivier, F. Rodriguez-Reinoso, J. Rouquerol and K. S. W. Sing, *Pure Appl. Chem.*, 2015, **87**, 1051–1069.

28 K. S. W. Sing, D. H. Everett, R. A. W. Haul, L. Moscou, R. A. Pierotti, J. Rouquerol and T. Siemieniewska, *Pure Appl. Chem.*, 1985, **57**, 603–619.

29 J. Zhang, M. Zhang, L. Lin and X. Wang, *Angew. Chemie - Int. Ed.*, 2015, **54**, 6297–6301.

30 J. Yu, K. Wang, W. Xiao and B. Cheng, *Phys. Chem. Chem. Phys.*, 2014, **16**, 11492.

31 L. Shi, T. Wang, H. Zhang, K. Chang and J. Ye, *Adv. Funct. Mater.*, 2015, **25**, 5360–5367.

32 B. W. Sun, H. Y. Yu, Y. J. Yang, H. J. Li, C. Y. Zhai, D. J. Qian and M. Chen, *Phys. Chem. Chem. Phys.*, 2017, **19**, 26072–26084.

33 F. Fina, S. K. Callear, G. M. Carins and J. T. S. Irvine, *Chem. Mater.*, 2015, **27**, 2612–2618.

34 T. Tyborski, C. Merschjann, S. Orthmann, F. Yang, M.-C. Lux-Steiner and T. Schedel-Niedrig, *J. Phys. Condens. Matter*, 2013, **25**, 395402.

35 J. Mao, T. Peng, X. Zhang, K. Li, L. Ye and L. Zan, *Catal. Sci. Technol.*, 2013, **3**, 1253.

36 S.-W. Cao, X.-F. Liu, Y.-P. Yuan, Z.-Y. Zhang, Y.-S. Liao, J. Fang, S. C. J. Loo, T. C. Sum and C. Xue, *Appl. Catal. B Environ.*, 2014, **147**, 940–946.

37 Y. Cao, Z. Zhang, J. Long, J. Liang, H. H. H. Lin, H. H. H. Lin and X. Wang, *J. Mater. Chem. A*, 2014, **2**, 17797–17807.

38 T. S. Miller, A. B. Jorge, T. M. Suter, A. Sella, F. Corà and P. F. McMillan, *Phys. Chem. Chem. Phys.*, 2017, **19**, 15613–15638.

39 S. Bai, X. Wang, C. Hu, M. Xie, J. Jiang and Y. Xiong, *Chem. Commun.*, 2014, **50**, 6094–6097.

40 M. J. Bojdys, J. O. Müller, M. Antonietti and A. Thomas, *Chem. - A Eur. J.*, 2008, **14**, 8177–8182.

41 X. Wang, K. Maeda, A. Thomas, K. Takanabe, G. Xin, J. M. Carlsson, K. Domen and M. Antonietti, *Nat. Mater.*, 2009, **8**, 76–80.

42 Q. Xiang, J. Yu and M. Jaroniec, *J. Phys. Chem. C*, 2011, **115**, 7355–7363.

43 J. Li, B. Shen, Z. Hong, B. Lin, B. Gao and Y. Chen, *Chem. Commun.*, 2012, **48**, 12017.

44 S. Min and G. Lu, *J. Phys. Chem. C*, 2012, **116**, 19644–19652.

45 A. B. Jorge, D. J. Martin, M. T. S. Dhanoa, A. S. Rahman, N. Makwana, J. Tang, A. Sella, F. Corà, S. Firth, J. A. Darr and P. F. McMillan, *J. Phys. Chem. C*, 2013, **117**, 7178–7185.

46 G. Socrates, *Infrared and Raman characteristic group frequencies. Tables and charts*, John Wiley & Sons Ltd, Chichester, Third., 2001.

47 P. Xia, B. Zhu, J. Yu, S. Cao and M. Jaroniec, *J. Mater. Chem. A*, 2017, **5**, 3230–3238.

48 J. Tian, L. Zhang, X. Fan, Y. Zhou, M. Wang, R. Cheng, M. Li, X. Kan, X. Jin, Z. Liu, Y. Gao and J. Shi, *J. Mater. Chem. A*, 2016, **4**, 13814–13821.

49   W.-J. Ong, L.-L. Tan, S.-P. Chai, S.-T. Yong and A. R. Mohamed, *Nano Energy*, 2015, **13**, 757–770.

50   K. Wang, Q. Li, B. Liu, B. Cheng, W. Ho and J. Yu, *Appl. Catal. B Environ.*, 2015, **176**–**177**, 44–52.

51   J. Hong, X. Xia, Y. Wang and R. Xu, *J. Mater. Chem.*, 2012, **22**, 15006–15012.

52   B. V Lotsch and W. Schnick, *Chem. Mater.*, 2005, **17**, 3976–3982.

53   V. W. Lau, I. Moudrakovski, T. Botari, S. Weinberger, M. B. Mesch, V. Duppel, J. Senker, V. Blum and B. V. Lotsch, *Nat. Commun.*, 2016, **7**, 12165.

54   R. C. Dante, P. Martín-Ramos, A. Correa-Guimaraes and J. Martín-Gil, *Mater. Chem. Phys.*, 2011, **130**, 1094–1102.

55   B. V Lotsch and W. Schnick, *Chem. Mater.*, 2006, **18**, 1891–1900.

56   J. Fu, B. Zhu, C. Jiang, B. Cheng, W. You and J. Yu, *Small*, 2017, **13**, 1603938.

57   H. Montigaud, B. Tanguy, G. Demazeau, I. Alves and S. Courjault, *J. Mater. Sci.*, 2000, **35**, 2547–2552.

58   D. R. Miller, J. Wang and E. G. Gillan, *J. Mater. Chem.*, 2002, **12**, 2463–2469.

59   S. Yang, Y. Gong, J. Zhang, L. Zhan, L. Ma, Z. Fang, R. Vajtai, X. Wang and P. M. Ajayan, *Adv. Mater.*, 2013, **25**, 2452–2456.

60   P. Larkin, *Infrared and Raman spectroscopy*, Elsevier, Amsterdam, Second., 2018.

61   F. Dong, Z. Wang, Y. Sun, W. K. Ho and H. Zhang, *J. Colloid Interface Sci.*, 2013, **401**, 70–79.

62   S. Zhou, Y. Liu, J. Li, Y. Wang, G. Jiang, Z. Zhao, D. Wang, A. Duan, J. Liu and Y. Wei, *Appl. Catal. B Environ.*, 2014, **158**–**159**, 20–29.

63   J. Xu, Y. Li, S. Peng, G. Lu and S. Li, *Phys. Chem. Chem. Phys.*, 2013, **15**, 7657.

64   H. Li, S. Gan, H. Wang, D. Han and L. Niu, *Adv. Mater.*, 2015, **27**, 6906–6913.

65   S. Hwang, S. Lee and J. S. Yu, *Appl. Surf. Sci.*, 2007, **253**, 5656–5659.

66   F. Dong, Z. Zhao, T. Xiong, Z. Ni, W. Zhang, Y. Sun and W. K. Ho, *ACS Appl. Mater. Interfaces*, 2013, **5**, 11392–11401.

67   Z. Wang, Y. Huang, L. Chen, M. Chen, J. Cao, W. Ho and S. C. Lee, *J. Mater. Chem. A*, 2018, **6**, 972–981.

68   F. Dong, L. Wu, Y. Sun, M. Fu, Z. Wu and S. C. Lee, *J. Mater. Chem.*, 2011, **21**, 15171.

69   J. Bian, J. Li, S. Kalytchuk, Y. Wang, Q. Li, T. C. Lau, T. A. Niehaus, A. L. Rogach and R. Q. Zhang, *ChemPhysChem*, 2015, **16**, 954–959.

70   Y. Yang, Y. Y. Guo, F. Liu, X. Yuan, Y. Y. Guo, S. Zhang, W. Guo and M. Huo, *Appl. Catal. B Environ.*, 2013, **142**–**143**, 828–837.

71   S. C. Yan, Z. S. Li and Z. G. Zou, *Langmuir*, 2009, **25**, 10397–10401.

72   X. Li, G. Hartley, A. J. Ward, P. A. Young, A. F. Masters and T. Maschmeyer, *J. Phys. Chem. C*, 2015, **119**, 14938–14946.

73   H. J. Li, B. W. Sun, L. Sui, D. J. Qian and M. Chen, *Phys. Chem. Chem. Phys.*, 2015, **17**, 3309–3315.

74   W. Yu, D. Xu and T. Peng, *J. Mater. Chem. A*, 2015, **3**, 19936–19947.

75   R. C. Dante, P. Martín-Ramos, A. Correa-Guimaraes and J. Martín-Gil, *Mater. Chem. Phys.*, 2011, **130**, 1094.

76   B. V. Lotsch, M. Döblinger, J. Sehnert, L. Seyfarth, J. Senker, O. Oeckler and W. Schnick, *Chem. - A Eur. J.*, 2007, **13**, 4969–4980.

77   E. Wirnhier, M. B. Mesch, J. Senker and W. Schnick, *Chem. - A Eur. J.*, 2013, **19**, 2041–2049.

78   T. Komatsu, *Macromol. Chem. Phys.*, 2001, **202**, 19–25.

79   J. Wen, J. Xie, X. Chen and X. Li, *Appl. Surf. Sci.*, 2017, **391**, 72–123.

80   W. J. Ong, L. K. Putri, Y. C. Tan, L. L. Tan, N. Li, Y. H. Ng, X. Wen and S. P. Chai, *Nano Res.*, 2017, **10**, 1673–1696.

81   J. Ma, C. Wang and H. He, *Appl. Catal. B Environ.*, 2016, **184**, 28–34.

82   J. Jiang, L. Ou-Yang, L. Zhu, A. Zheng, J. Zou, X. Yi and H. Tang, *Carbon*, 2014, **80**, 213–221.

83   W.-J. Ong, L.-L. Tan, S.-P. Chai and S.-T. Yong, *Dalt. Trans.*, 2015, **44**, 1249–1257.

84   S. Wan, M. Ou, X. Wang, Y. Wang, Y. Zeng, J. Ding, S. Zhang and Q. Zhong, *Dalt. Trans.*, 2019, **48**, 12070–12079.

85   Z. Pan, P. Niu, M. Liu, G. Zhang, Z. Zhu and X. Wang, *ChemSusChem*, 2020, **13**, 888–892.

86   T. Giannakopoulou, I. Papailias, N. Todorova, N. Boukos, Y. Liu, J. Yu and C. Trapalis, *Chem. Eng. J.*, 2017, **310**, 571–580.

87   Z. A. Lan, G. Zhang and X. Wang, *Appl. Catal. B Environ.*, 2016, **192**, 116–125.

88   P. F. McMillan, V. Lees, E. Quirico, G. Montagnac, A. Sella, B. Reynard, P. Simon, E. Bailey, M. Deifallah and F. Corà, *J. Solid State Chem.*, 2009, **182**, 2670–2677.

89   D. J. Martin, K. Qiu, S. A. Shevlin, A. D. Handoko, X. Chen, Z. Guo and J. Tang, *Angew. Chemie - Int. Ed.*, 2014, **53**, 9240–9245.

90   M. Zhang, Y. Duan, H. Jia, F. Wang, L. Wang, Z. Su and C. Wang, *Catal. Sci. Technol.*, 2017, **7**, 452–458.

91   Z. Zhu, X. Tang, T. Wang, W. Fan, Z. Liu, C. Li, P. Huo and Y. Yan, *Appl. Catal. B Environ.*, 2019, **241**, 319–328.

92   M. Zhang, X. Bai, D. Liu, J. Wang and Y. Zhu, *Appl. Catal. B Environ.*, 2015, **164**, 77–81.

93   G. Li, J. Shi, G. Zhang, Y. Fang, M. Anpo and X. Wang, *Res. Chem. Intermed.*, 2017, **43**, 5137–5152.

94   J. Xu, L. Zhang, R. Shi and Y. Zhu, *J. Mater. Chem. A*, 2013, **1**, 14766.

95   A. Kumar, P. Kumar, R. Borkar, A. Bansiwal, N. Labhsetwar and S. L. Jain, *Carbon*, 2017, **123**, 371–379.

96   E. Quirico, G. Montagnac, V. Lees, P. F. McMillan, C. Szopa, G. Cernogora, J. N. Rouzaud, P. Simon, J. M. Bernard, P. Coll, N. Fray, R. D. Minard, F. Raulin, B. Reynard and B. Schmitt, *Icarus*, 2008, **198**, 218–231.

97   A. C. Ferrari, S. E. Rodil, J. Robertson, S. E. Rodil and J. Robertson, *Phys. Rev. B - Condens. Matter Mater. Phys.*, 2003, **67**, 155306.

98 M. Z. Rahman, P. C. Tapping, T. W. Kee, R. Smernik, N. Spooner, J. Moffatt, Y. Tang, K. Davey and S. Z. Qiao, *Adv. Funct. Mater.*, 2017, **27**, 1702384.

99 S. Wood, J. R. Hollis and J.-S. Kim, *J. Phys. D. Appl. Phys.*, 2017, **50**, 073001.

100 A. E. Bragg, W. Yu, J. Zhou and T. Magnanelli, *J. Phys. Chem. Lett.*, 2016, **7**, 3990–4000.

101 L. K. Putri, W. J. Ong, W. S. Chang and S. P. Chai, *Catal. Sci. Technol.*, 2016, **6**, 744–754.

102 W. Tang, Y. Tian, B. Chen, Y. Xu, B. Li, X. Jing, J. Zhang and S. Xu, *ACS Appl. Mater. Interfaces*, 2020, **12**, 6396–6406.

103 J.-C. Wang, H.-C. Yao, Z.-Y. Fan, L. Zhang, J.-S. Wang, S.-Q. Zang and Z.-J. Li, *ACS Appl. Mater. Interfaces*, 2016, **8**, 3765–3775.

104 C. Zhou, C. Lai, D. Huang, G. Zeng, C. Zhang, M. Cheng, L. Hu, J. Wan, W. Xiong, M. Wen, X. Wen and L. Qin, *Appl. Catal. B Environ.*, 2018, **220**, 202–210.

105 S. W. Cao, Y. P. Yuan, J. Fang, M. M. Shahjamali, F. Y. C. Boey, J. Barber, S. C. Joachim Loo and C. Xue, *Int. J. Hydrogen Energy*, 2013, **38**, 1258–1266.

106 W. Xing, G. Chen, C. Li, Z. Han, Y. Hu and Q. Meng, *Nanoscale*, 2018, **10**, 5239–5245.

107 Q. Huang, J. Yu, S. Cao, C. Cui and B. Cheng, *Appl. Surf. Sci.*, 2015, **358**, 350–355.

108 M. Li, S. Zhang, X. Liu, J. Han, X. Zhu, Q. Ge and H. Wang, *Eur. J. Inorg. Chem.*, 2019, **2019**, 2058–2064.

109 J. F. Moulder, J. Chastain, W. F. Stickle, P. E. Sobol and K. D. Bomben, *Handbook of x-ray photoelectron spectroscopy : a reference book of standard spectra for identification and interpretation of XPS data,* Physical Electronics Division, Perkin-Elmer Corporation, 1992.

110 W. Li, Y. Hu, E. Rodríguez-Castellón and T. J. Bandosz, *J. Mater. Chem. A*, 2017, **5**, 16315–16325.

111 J. Barrio, L. Lin, X. Wang and M. Shalom, *ACS Sustain. Chem. Eng.*, 2018, **6**, 519–530.

112 X. Li, G. Hartley, A. J. Ward, P. A. Young, A. F. Masters and T. Maschmeyer, *J. Phys. Chem. C*, 2015, **119**, 14938.

113 M. Taheri, M. Ghiaci and A. Shchukarev, *Appl. Organomet. Chem.*, 2018, **32**, e4338.

114 X. Kang, Y. Kang, X. Hong, Z. Sun, C. Zhen, C. Hu, G. Liu and H. Cheng, *Prog. Nat. Sci. Mater. Int.*, 2018, **28**, 183.

115 E. Vorobyeva, Z. Chen, S. Mitchell, R. K. Leary, P. Midgley, J. M. Thomas, R. Hauert, E. Fako, N. López and J. Pérez-Ramírez, *J. Mater. Chem. A*, 2017, **5**, 16393.

116 B. Yue, Q. Li, H. Iwai, T. Kako and J. Ye, *Sci. Technol. Adv. Mater.*, 2011, **12**, 034401.

117 N. Hellgren, R. T. Haasch, S. Schmidt, L. Hultman and I. Petrov, *Carbon*, 2016, **108**, 242.

118 J. Wu, N. Li, X.-H. Zhang, H.-B. Fang, Y.-Z. Zheng and X. Tao, *Appl. Catal. B Environ.*, 2018, **226**, 61.

119 Z. Teng, W. Cai, S. Liu, C. Wang, Q. Zhang, S. Chenliang and T. Ohno, *Appl. Catal. B Environ.*, 2020, **271**, 118917.

120 G. Shi, L. Yang, Z. Liu, X. Chen, J. Zhou and Y. Yu, *Appl. Surf. Sci.*, 2018, **427**, 1165–1173.

121 J. T. Yin, Z. Li, Y. Cai, Q. F. Zhang and W. Chen, *Chem. Commun.*, 2017, **53**, 9430–9433.

122 Y. Li, W. Ho, K. Lv, B. Zhu and S. C. Lee, *Appl. Surf. Sci.*, 2018, **430**, 380–389.

123 G. Dong and L. Zhang, *J. Mater. Chem.*, 2012, **22**, 1160–1166.

124 T. Song, P. Zhang, J. Zeng, T. Wang, A. Ali and H. Zeng, *ChemCatChem*, 2017, **9**, 4035–4042.

125 M. Li, H. Wang, X. Li, S. Zhang, J. Han, A. F. Masters, T. Maschmeyer and X. Liu, *ChemCatChem*, 2018, **10**, 581–589.

126 Z. Shu, Y. Wang, W. Wang, J. Zhou, T. Li, X. Liu, Y. Tan and Z. Zhao, *Int. J. Hydrogen Energy*, 2019, **44**, 748–756.

127 B. Jürgens, E. Irran, J. Senker, P. Kroll, H. Müller and W. Schnick, *J. Am. Chem. Soc.*, 2003, **125**, 10288–10300.

128 J. C. Sánchez-López, C. Donnet, F. Lefèbvre, C. Fernéndez-Ramos and A. Fernández, *J. Appl. Phys.*, 2001, **90**, 675–681.

129 D. L. B. Robert M. Silverstein, Francis X. Webster, David J. Kiemle, *Spectrometric Identification of Organic Compounds*, John Wiley & Sons, Ltd, Chichester, 8th edn., 2014.

130 S. A. Richards and J. C. Hollerton, *Essential Practical NMR for Organic Chemistry | Wiley*, John Wiley & Sons, Ltd, Chichester, First., 2011.

131 M. Li, L. Zhang, X. Fan, Y. Zhou, M. Wu and J. Shi, *J. Mater. Chem. A*, 2015, **3**, 5189–5196.

132 F. Dong, Z. Zhao, T. Xiong, Z. Ni, W. Zhang, Y. Sun and W.-K. K. Ho, *ACS Appl. Mater. Interfaces*, 2013, **5**, 11392–11401.

133 H. Shi, G. Chen, C. Zhang and Z. Zou, *ACS Catal.*, 2014, **4**, 3637–3643.

134 G. Zhang, M. Zhang, X. Ye, X. Qiu, S. Lin and X. Wang, *Adv. Mater.*, 2014, **26**, 805–809.

135 H. Shi, S. Long, J. Hou, L. Ye, Y. Sun, W. Ni, C. Song, K. Li, G. G. Gurzadyan and X. Guo, *Chem. – A Eur. J.*, 2019, **25**, 5028–5035.

136 M. S. Akple, T. Ishigaki and P. Madhusudan, *Environ. Sci. Pollut. Res.*, 2020, **27**, 22604–22618.

137 M. Shen, L. Zhang, M. Wang, J. Tian, X. Jin, L. Guo, L. Wang and J. Shi, *J. Mater. Chem. A*, 2019, **7**, 1556–1563.

138 Z. Zhang, J. Huang, M. Zhang, Q. Yuan and B. Dong, *Appl. Catal. B Environ.*, 2015, **163**, 298–305.

139 P. Niu, L. Zhang, G. Liu and H. M. Cheng, *Adv. Funct. Mater.*, 2012, **22**, 4763–4770.

140 X. Wang, S. Blechert and M. Antonietti, *ACS Catal.*, 2012, **2**, 1596–1606.

141 L. Lin, C. Hou, X. Zhang, Y. Wang, Y. Chen and T. He, *Appl. Catal. B Environ.*, 2018, **221**, 312–319.

142 F. Shao, L. Mi, Z. Tian, C. Zheng, Y. Zhang, Q. Li and S. Liu, *ACS Appl. Mater. Interfaces*, 2019, **11**, 44922–44930.

143 W. Li, X. He, R. Ge, M. Zhu, L. Feng and Y. Li, *Sustain. Mater. Technol.*, 2019, **22**, e00114.

144 P. Chanhom, N. Charoenlap, C. Manipuntee and N. Insin, *J. Magn. Magn. Mater.*, 2019, **475**, 602–610.

145 D. Chen, K. Wang, W. Hong, R. Zong, W. Yao and Y. Zhu, *Appl. Catal. B Environ.*, 2015, **166**–**167**, 366–373.

146 S. Mei, J. Gao, Y. Zhang, J. Yang, Y. Wu, X. Wang, R. Zhao, X. Zhai, C. Hao, R. Li and J.

Yan, *J. Colloid Interface Sci.*, 2017, **506**, 58–65.

147   X. Zhang, L. Lin, D. Qu, J. Yang, Y. Weng, Z. Wang, Z. Sun, Y. Chen and T. He, *Appl. Catal. B Environ.*, 2020, **265**, 118595.

148   G. Zhao, H. Pang, G. Liu, P. Li, H. Liu, H. Zhang, L. Shi and J. Ye, *Appl. Catal. B Environ.*, 2017, **200**, 141–149.

149   G. Neri, M. Forster, J. J. Walsh, C. M. Robertson, T. J. Whittles, P. Farràs and A. J. Cowan, *Chem. Commun.*, 2016, **52**, 14200–14203.